Modeling Oxidative Dehydrogenation of Propane with Supported Vanadia Catalysts Using Multireference Methods

Mukunda Mandal [*,†] Matthew R. Hermes [†] Fabian Berger [‡,¶] Joachim Sauer [‡] and Laura Gagliardi [*,†,§]

†*Department of Chemistry, Chicago Center for Theoretical Chemistry, University of Chicago, Chicago, Illinois 60615, United States*

‡*Institut für Chemie, Humboldt-Universität zu Berlin, Berlin 10099, Germany*

¶*Present address: Yusuf Hamied Department of Chemistry, University of Cambridge, CB2 1EW Cambridge, United Kingdom*

§*Pritzker School of Molecular Engineering, The James Franck Institute, University of Chicago, Chicago, Illinois 60615, United States*

E-mail: mukunda.chem@gmail.com; lgagliardi@uchicago.edu

Abstract

The oxidative dehydrogenation of propane over supported vanadium oxide catalysts poses significant computational challenges due to complex electronic structure changes along the reaction coordinate, driven primarily by changes in the oxidation states of vanadium. To address these challenges, we systematically test quantum chemical methods, including multireference (MR) approaches, domain-based local pair natural orbital coupled cluster theory (DLPNO-CCSD(T)), and density functional theory (DFT). The initial C–H bond-breaking transition state requires MR treatment due to its multireference character, while subsequent steps permit efficient single-reference calculations. For the rate-limiting C–H activation step mediated by the vanadyl moiety, complete

active space second-order perturbation theory (CASPT2) yields an apparent activation barrier ($E_{\mathrm{app}}^{600\mathrm{K}}$) of 138 kJ/mol, consistent with experimental values (134 ± 4 kJ/mol; Gruene et al. *Catal. Today* **2010**, *157*, 137). In contrast, DLPNO-CCSD(T) overestimates this barrier (198 kJ/mol), whereas DFT predictions span 125–150 kJ/mol, depending on the functional. Our multireference investigation of this transition metal oxide-catalyzed process demonstrates that an active space that incorporates the C–H σ and V=O σ/π bonding orbitals, oxygen lone pairs, and their antibonding counterparts adequately captures electronic structure changes along the chemical transformation. These findings provide a general strategy for active space selection in transition metal oxide-catalyzed C/O–H bond activation reactions. The reference dataset from this work, which includes MR calculations with manually selected active spaces for all intermediates and transition states in the propane ODH reaction network, will serve as a benchmark for automating active space selection in similar systems.

I. Introduction

Light olefins, particularly propene, serve as crucial building blocks in the chemical industry.[1–3] While propene has traditionally been produced through petroleum cracking, oxidative dehydrogenation (ODH) of propane has emerged as a promising alternative method for its production.[4,5] Among the most widely studied catalysts for this transformation are supported vanadium oxide (VO_x) systems, especially silica-supported vanadia species (VO_x/SiO_2).[6–8]

On VO_x catalysts, propane ODH proceeds via the Mars-van Krevelen (MvK) redox mechanism, wherein V^V mediates the rate-limiting C–H bond activation, generating propene while being reduced to V^{III}.[9,10] The catalytic cycle concludes as O_2 rapidly re-oxidizes V^{III} back to V^V—a process $\sim 10^5$ times faster than propane oxidation,[11,12] effectively decoupling catalyst regeneration from the rate-determining substrate activation.[13,14]

Beyond its industrial significance, propane ODH serves as an important model system for studying C–H bond activation, a fundamental process in both catalysis and enzymatic reactions. Mechanistic understanding of this chemistry requires accurate computational methods to complement experimental insights. While density functional theory (DFT) is efficient and often sufficiently accurate, its single-determinant framework fails to fully capture the complex electronic structure changes inherent in these oxidation processes. This limitation highlights the need for computational methods that can better account for electron correlation effects

in such systems.

Multireference (MR) quantum chemical methods can describe electronic structures with significant static correlation, accurately capturing near-degenerate electronic states commonly encountered in C–H activation reactions, especially at transition structures.[15] Even with their computational demands and the expertise needed to define active spaces, MR methods have proven essential for understanding critical aspects of catalytic mechanisms.[16,17] These include mechanistic insights into C–H activation in propane on bimetallic oxide clusters,[18,19] methane-to-methanol conversion across enzyme-mimicking models, synthetic frameworks, and Fe-based molecular catalysts,[20,21] as well as Ni-catalyzed C–H arylation[22] and Cu-catalyzed C–C coupling reactions.[23]

In modeling metal oxide-catalyzed propane ODH reactivity, computational studies have relied predominantly on DFT.[14,24–27] However, higher-level calculations have shown notable limitations in DFT-based approaches. For instance, in methane activation by VO^+, B3LYP[28,29] predicted the first hydrogen abstraction barrier approximately 50 kJ/mol lower than multireference configuration interaction (MRCI+Q) benchmark values.[30] Similarly, coupled cluster (CCSD(T)) calculations on a $O{=}V(OH)_3$ model demonstrated that B3LYP underestimates this barrier for C1–C3 alkanes by 40–60 kJ/mol compared to CCSD(T).[31] These studies highlight the importance of applying both single-reference and multireference wave function methods to supported VO_x catalyst models to gain a reliable mechanistic understanding of propane ODH reactivity.

In this work, we employ a representative silica cluster model ($O{=}VSi_7O_{12}H_7$) to analyze the mechanism of propane ODH over silica-supported vanadia catalysts. Our approach combines multireference (MR) methods such as complete active space self-consistent field (CASSCF),[32] its perturbation theory extension (CASPT2),[33] and multiconfiguration pair-density functional theory (MC-PDFT),[34] with single-reference methods like domain-based local pair natural orbital (DLPNO) CCSD(T)[35] and various Kohn-Sham density functionals. Previous studies of propane ODH catalysis using well-defined cluster models like $O{=}VSi_7O_{12}H_7$ have been limited to DFT, whereas wave function methods have only been applied to minimal model systems such as VO^+ and $O{=}V(OH)_3$.[30,31] We bridge this gap by performing calculations with various electronic structure methods on the same $O{=}VSi_7O_{12}H_7$ model system, which provides a more realistic representation of the catalytic environment.[14,36] Analyzing each step of propane ODH in detail, we find that the initial C–H

bond cleavage transition state exhibits pronounced MR character, requiring MR methods for accurate results. In subsequent steps, where MR character diminishes, single-reference methods remain sufficiently reliable. We also investigate support-assisted reaction pathways and demonstrate how the oxide support may influence reactivity. Our MR benchmark data, based on manually selected active spaces, will serve as a reference for future development of automated active space selection protocols and broader studies of metal oxide-catalyzed reactions involving complex coordination and oxidation state changes.

II. Model Systems

To balance accuracy with computational feasibility, we adopted a molecular model previously employed in studies of propane ODH over supported vanadia catalysts.[36–39] The silica support was represented by a cubic silsesquioxane cluster ($Si_8O_{12}H_8$, **1**; Figure 1a), featuring tetrahedral Si centers that effectively mimic the [SiO_4] units characteristic of silica surfaces. Terminal hydrogens cap the dangling bonds, ensuring a closed-shell configuration. The active site was modeled as $O{=}VSi_7O_{12}H_7$ (**2**; Figure 1b), created by replacing a Si–H bond at one vertex of **1** with a vanadyl (V=O) group. This model also reflects experimental observations of isolated VO_4 species at low vanadium loadings on silica, which adopt distorted tetrahedral or pyramidal geometries under dehydrated conditions.[40,41] Featuring fused $(Si{-}O)_4$ rings, this model combines structural rigidity with sufficient local flexibility to accommodate local relaxations at reaction sites. By remaining computationally tractable, the model allows us to apply high-level wave function-based methods and systematically evaluate the performance of different theoretical approaches.[14,39]

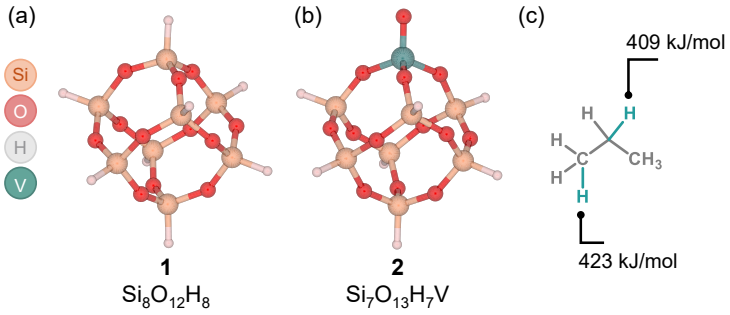

Figure 1: Catalytic models studied: (a) cubic silica support $Si_8O_{12}H_8$ (**1**); (b) VO_x active site $O{=}VSi_7O_{12}H_7$ (**2**); (c) propane substrate with experimental primary and secondary C–H bond dissociation enthalpies (BDEs) from Ref.[42]

III. Results and Discussion

Before presenting our computational results, we briefly summarize reported experimental apparent activation energies (E_{app}) for propane ODH over silica-supported vanadia catalysts. These values, typically derived from fitting the temperature dependence of the reaction rate to the Arrhenius equation,[43,44] vary significantly due to the structural heterogeneity of the catalysts and the sensitivity of activation energies to catalyst preparation methods and support characteristics. Carrero et al. analyzed a wide range of published literature on experimental activation energies and derived an average activation barrier of 117 ± 28 kJ/mol for V_2O_5/SiO_2 catalysts.[12] This large range underscores the influence of active site composition and distribution on reactivity, as well as the experimental challenges in establishing clear structure/activity relationships.

To provide specific examples, several studies have reported apparent activation energies under varying experimental conditions. For instance, V_2O_5/SiO_2 catalysts with vanadium surface coverages below 0.5 V/nm^2 (MCM-41) exhibit apparent activation energies of 122 ± 20 kJ/mol.[14,45] Similarly, vanadia catalysts supported on mesoporous, microporous, and non-porous silica have shown values in the range of 120–140 kJ/mol.[46] At 400 °C, low-loaded (<2 V/nm^2) V_xO_y/SiO_2 catalysts prepared via saturation wetness impregnation demonstrate activation barriers of 146 ± 6 kJ/mol,[8] while under comparable low-loading conditions, V_xO_y/SiO_2 catalysts supported on mesoporous silica SBA-15 exhibit a barrier of approximately 134 ± 4 kJ/mol.[47] Given the ordered nature and thermal stability of the SBA-15 support,[48] we use these latter data (134 ± 4 kJ/mol), as a point of comparison for our computational results.

Building on the observed variation in experimental activation energies and previous computational studies, we employ DFT and wave function-based methods to examine propane ODH over V/SiO_2 catalysts. While earlier work, such as that by Rozanska et al., provided valuable insights into the mechanism and identified several plausible routes to propene formation using the silsesquioxane model O=$VSi_7O_{12}H_7$ (**2**; Figure 1b), these studies often relied on correction factors to account for dispersion interactions in van der Waals complexes.[14,24] To overcome this limitation, we optimize stationary point geometries at the M06-D3(0)/def2-TZVP level, a method that incorporates dispersion effects and has been validated for both supported vanadia catalysis and C–H activation reaction pathways.[49,50] While most of the

mechanistic pathways explored here align with prior work,[14,24,25] we propose a previously unreported intermediate that may play a role in understanding ODH selectivity limitations, as we explore in detail in the following text.

IIIA. Reaction Mechanism

We analyze the mechanism of propane-to-propene oxidation in three parts. First, we examine activation of the secondary C–H bond in propane to form an isopropyl radical (Paths A and B; Figure 2). This is followed by two possible reaction pathways for the conversion of the radical to propene: single-site pathways (SSPs), where all steps occur at a single VO_x center (Paths C to F; Figure 5a) and a cooperative mechanism involving multiple neighboring VO_x sites (Path G; Figure 5c)

For the initial C–H activation, we benchmark computational results against experimental kinetics,[47] while for subsequent steps, where experimental data are unavailable, we use CASPT2 as a reference, justified by its ability to account for both static and dynamic correlation in transition-metal systems with multireference character.[15,17,51]

IIIA.1. Initial C–H Activation

The reaction begins with the formation of a weak van der Waals complex (INT-1; Figure 2) between propane and the catalyst. The secondary C–H bond of propane can then be activated through two possible pathways: Path A involves a bridging Si–O–V oxygen atom (TS-12), forming INT-2 that comprises an isopropyl radical ($CH_3CH(\bullet)CH_3$), a surface –OH group, and an $O{=}V^{IV}(–O)_2(\bullet)$ fragment. Alternatively, Path B proceeds via the vanadyl oxygen (O=V; TS-13), forming INT-3, in which the isopropyl radical is weakly stabilized at a V^{IV}–OH site. Both intermediates (INT-2 and INT-3) adopt a triplet electronic configuration, which remains the lowest-energy state for all intermediates and transition states along the subsequent single-site pathways.

At the DLPNO-CCSD(T) level, INT-1 is only marginally stabilized ($\Delta H_{600K}^{(\text{INT-1 – INT-0})} = –$ 3 kJ/mol). The apparent activation barrier $E_{app}^{TS-n}(T)$ is calculated as the enthalpy difference between TS-n and INT-0, corrected by the thermal term RT: $E_{app}^{TS-n}(T) = H^{TS-n}(T) – H^{INT\text{-}0}(T) + RT$.[43,44] Using this expression, the calculated E_{app}^{600K} values for TS-12 and TS-13 are 234 and 198 kJ/mol, respectively, indicating that Path B is favored over Path A by

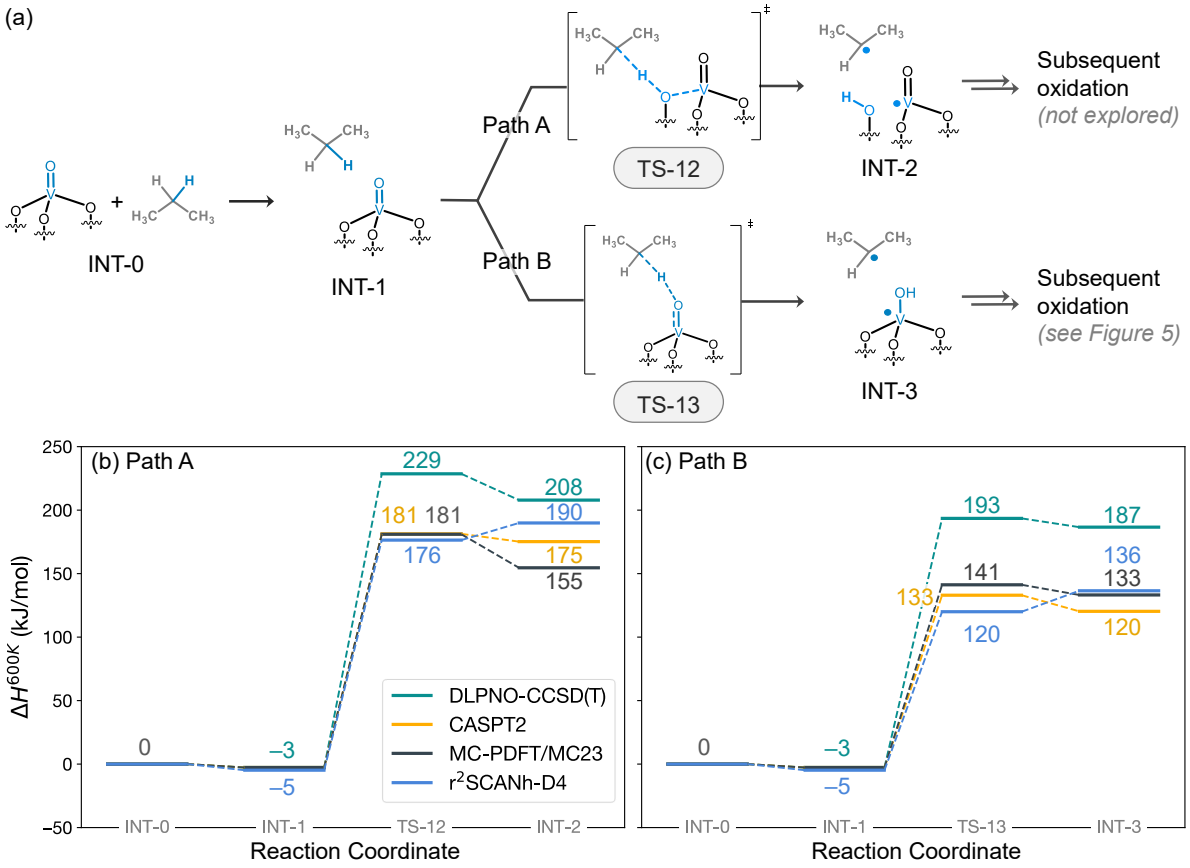

Figure 2: Initial C–H activation in propane ODH catalyzed by O=$VSi_7O_{12}H_7$ (**2**). (a) Reaction pathways via bridging oxygen (Path A) and vanadyl oxygen (Path B). (b,c) Enthalpy profiles (kJ/mol, 600 K, relative to INT-0) for Paths A and B, respectively; Path B is kinetically preferred. Energies computed at DLPNO-CCSD(T) (green), CASPT2 (yellow), MC-PDFT/MC23 (black), and r^2SCANh-D4 (blue) using M06-D3(0)/def2-TZVP geometries. CASPT2 and MC-PDFT use a CASSCF(8*e*,8*o*) reference. Spin states: INT-0/1 (closed-shell singlets), TS-12/13 (open-shell singlets), INT-2/3 (triplets). (Note on stationary point labels: TS-xy denotes a transition state connecting INT-x and INT-y.)

36 kJ/mol (Figure 2b,c). Two factors may contribute to the preference for Path B: the greater nucleophilicity of the vanadyl oxygen (partial charges of –0.569 *e* vs. –0.505 *e* for the bridging oxygen, calculated using Charge Model 5),[52] and the more favorable formation of a V–O σ bond from a V=O π bond (as in INT-3), relative to breaking a pre-existing V–O σ bond in the support (as in INT-2), as reflected in the ∼20 kJ/mol lower enthalpy of INT-3 relative to INT-2.

As discussed in later sections, this initial C–H activation is the rate-limiting step of the overall ODH process, consistent with both experimental kinetics and computed energy profiles.[14] However, the DLPNO-CCSD(T) barrier for TS-13 ($E_{\mathrm{app}}^{600\mathrm{K}}$ = 198 kJ/mol) significantly

overestimates the experimental activation energy of 134 ± 4 kJ/mol.[47] This discrepancy suggests that single-reference coupled-cluster theory does not fully capture the open-shell singlet character of the C–H bond-breaking transition state, motivating the use of multireference methods for more accurate description.

To probe the multireference character of the rate-limiting C–H activation step, we performed CASSCF calculations along the intrinsic reaction coordinate (IRC) of TS-13. The Supporting Information details the active space selection, with CAS(8*e*,8*o*) identified as optimal for capturing the relevant electronic structure while avoiding active space inconsistency errors. For TS-13, this space includes the V=O σ and π bonding/antibonding orbitals, the C–H σ bonding/antibonding pair, an oxygen lone pair interacting with the vanadium 3*d* shell, and an additional unoccupied V(3*d*) orbital (Figure S2).

The evolution of natural orbital occupation numbers (NOONs) along the IRC provides clear evidence of static correlation. As the reaction progresses toward isopropyl radical formation, the NOON of the filled V=O π/C–H σ bonding orbital decreases from 1.93 to 1.12, while that of the formerly unoccupied V(3*d*) orbital rises from 0.07 to 0.88. Near the C–H bond cleavage transition state (Point "C"; Figure 3), both orbitals exhibit significant partial occupancy (1.51 and 0.49, respectively), reflecting strong static electron correlation not captured by single-reference methods. By contrast, the reactant and product regions display near-closed-shell behavior, with occupation numbers close to 2.0/0.0 or 1.0/1.0, respectively.

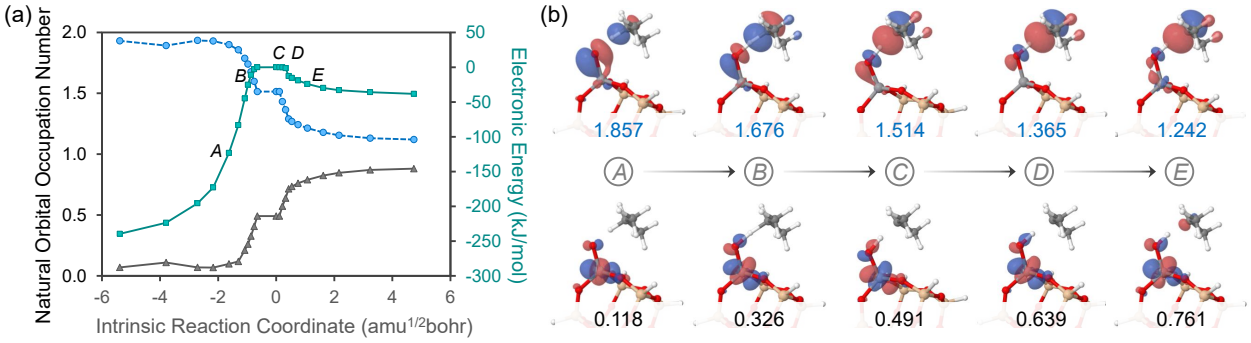

Figure 3: Electronic structure changes along the intrinsic reaction coordinate (IRC) for vanadyl-mediated C–H activation (Path B; Figure 2). (a) CASSCF(8*e*,8*o*) single-point energies computed on M06-D3(0)/def2-TZVP IRC geometries (green solid line). Natural orbital occupation numbers (NOONs) show the evolution of an occupied V=O π/C–H σ bond into a C(2*p*) orbital (blue dashed line) and an empty V(3*d*) orbital into a singly occupied V(3*d*) orbital (grey solid line). (b) Representative natural orbital diagrams showing the two most significantly evolving orbitals during the reaction, with corresponding NOONs at selected IRC points.

These findings motivated the use of second-order multireference perturbation theory to obtain more accurate energetics. CASPT2 calculations based on the CAS(8e,8o) reference yielded apparent barriers of 186 and 138 kJ/mol for TS-12 and TS-13, respectively (Figure 2b,c). N-electron valence state second-order perturbation theory (NEVPT2) yielded slightly lower values, at 173 and 115 kJ/mol, respectively, but both methods consistently favor the vanadyl-mediated pathway (Path B) by 50 to 60 kJ/mol over the bridging-oxygen route (Path A), consistent with trends observed at the coupled-cluster level. Notably, unlike DLPNO-CCSD(T), the CASPT2 barrier for TS-13 closely matches the experimental value of 134 ± 4 kJ/mol,[47] demonstrating the importance of multireference methods for accurately describing this system.

We next employed MC-PDFT as a more efficient approach for capturing both static and dynamic correlation, testing three on-top functionals using the CAS(8e,8o) reference (Table 1). While tPBE[34] significantly underestimates the apparent activation barrier for TS-13 ($E_{\mathrm{app}}^{600\mathrm{K}} = 88$ kJ/mol), hybrid tPBE0 (containing 25% CASSCF energy)[53] and the recently developed hybrid meta functional MC23[54] yield more accurate barriers of 122 and 146 kJ/mol, respectively, with MC23 closely reproducing the CASPT2 result of 138 kJ/mol.

Turning to more widely accessible methods, we evaluated the performance of four hybrid Kohn-Sham density functionals. Among these, r^{2}SCANh-D4, TPSSh-D4, and ωB97M-D4 predict apparent barriers of 125, 133, and 143 kJ/mol, respectively, in good agreement with the CASPT2 result. In contrast, M06-D3(0) slightly overestimates the barrier, yielding 153 kJ/mol. Despite their favorable barrier heights, both r^{2}SCANh-D4 and TPSSh-D4 exhibit notable inconsistencies in the energy landscape, placing INT-3 approximately 15 to 25 kJ/mol above the preceding transition state TS-13, as shown in Figure 2b,c and summarized in Table 1. This artifact arises because electronic energies are evaluated using the respective functionals, while all geometries and thermal corrections are computed at the M06-D3(0)/def2-TZVP level.

Our analysis of the initial C–H activation step identifies Path B, involving vanadyl oxygen, as the preferred route, consistent with O^{18} isotope-labeling experiments[55] and prior computational studies reporting similar barrier differences ($\Delta\Delta H_{0\mathrm{K(A–B)}}^{\ddagger} = 38$ to 60 kJ/mol).[14,25] While single-reference DLPNO-CCSD(T) overestimates the barrier (198 kJ/mol), multireference CASPT2 calculations (138 kJ/mol) closely match the experimental value (134 ± 4 kJ/mol),[47] and alternative multireference approaches such as NEVPT2 and MC-PDFT (notably, tPBE0

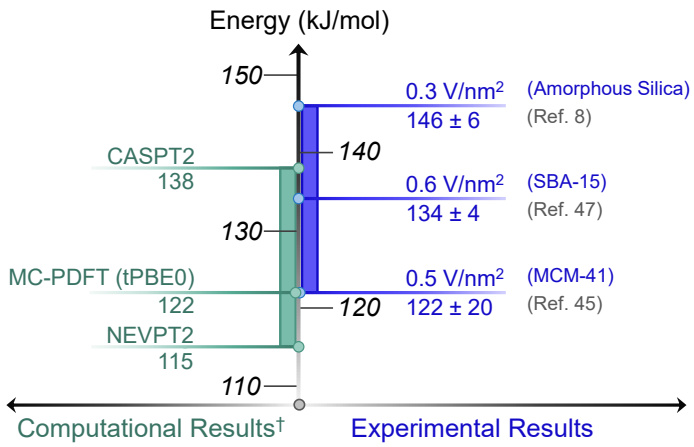

Figure 4: Comparison of experimentally determined apparent activation barriers with computed activation enthalpies (600 K; †using CAS(8*e*,8*o*) reference) for the rate-limiting initial C–H activation step using select multireference methods with the silsesquioxane cluster model ($Si_7O_{13}H_7V$). Experimental apparent activation barriers are obtained from references:[8,45,47]

and MC23) yield similarly reliable barriers (Figure 4). These results demonstrate that accurate description of the transition state in this open-shell system requires explicit treatment of static correlation, highlighting the limitations of single-reference methods. In this context, it is noteworthy that our model describes isolated vanadyl species, although experimental catalysts likely contain a distribution of monomeric, dimeric, and oligomeric sites, with dimeric species potentially exhibiting lower barriers.[24]

IIIA.2. Reactivity of the Isopropyl Radical along Single-Site Pathways (SSP)

With Path B established as the preferred route for C–H activation, we next examine the reactivity of the resulting isopropyl radical intermediate, INT-3. This species can undergo further oxidation via several competing single-site pathways, as outlined in Figure 5a. To frame the discussion, we first describe the reaction network based on stationary points and their connectivity. We then analyze the extent of MR character along each pathway and benchmark the associated energetics using CASPT2 and MC-PDFT, followed by a comparison with DLPNO-CCSD(T) and Kohn-Sham DFT results.

The isopropyl radical intermediate can proceed through two general mechanistic classes: direct hydrogen-atom abstraction (HAA; Paths C and E; Figure 5a) or radical recombination followed by rearrangement (Paths D and F). In the single-site direct HAA routes, a second C–H activation occurs at the methyl group of $CH_3CH(\bullet)CH_3$ via either a V^{IV}–OH moiety (TS-

34, Path C) or a bridging oxygen (TS-35, Path E). These transition structures respectively lead to INT-4, where propene forms alongside a water-bound, reduced V^{III} species, and INT-5, where hydrogen transfers to a bridging oxygen, cleaving the V–O(Si) bond.

In the radical recombination routes, the isopropyl radical binds to a hydroxyl group from V^{IV}–OH (TS-37, Path D) or to a bridging oxygen (TS-36, Path F), forming either INT-7, a reduced $V^{III}(–O)_3$ species with coordinated 2-propanol, or INT-6, comprising Si–$OC(H)(CH_3)_2$ and $V^{III}(OH)(–O)_2$. Both intermediates (INT-6 and INT-7) undergo further transformation through cyclic transition states TS-64 and TS-75, ultimately converging to INT-4 and INT-5, respectively. The V^{III}–OH moiety in INT-5 can eventually abstract a proton from a surface HO–Si via TS-54, merging into INT-4. INT-4 is then reoxidized by O_2, completing the catalytic cycle;[11,12] however, we do not model these reoxidation steps in the current work. For further discussion of catalyst reoxidation in related systems, we refer readers to prior studies employing Kohn-Sham DFT.[25]

Additionally, we identify a previously unreported intermediate, INT-10, featuring a V^{III} center analogous to INT-4 but coordinating propene instead of water. The energetic and mechanistic implications of INT-10 are discussed below.

IIIA.2.1. Multireference Diagnostics for the Reaction Network. As in the initial C–H activation step, we used two diagnostics, T_1 and M, to systematically explore MR character along the reaction pathways. The T_1 diagnostic, derived from coupled-cluster t_1 amplitudes, signals strong static correlation when it exceeds 0.02 for closed-shell or 0.045 for open-shell species.[56] However, T_1 is known to underestimate MR character in certain transition-metal systems.[57] To address this limitation, we also employed the M diagnostic, which quantifies deviation from ideal single-reference behavior based on natural orbital occupation numbers (see Equation S2).[58] According to this metric, MR character is considered low ($M < 0.05$), moderate ($0.05 < M < 0.1$), or high ($M > 0.1$).[59]

Diagnostic results (Table S1) confirm and extend the natural orbital occupation analysis presented earlier in Figure 3. Most intermediates exhibit T_1 values below 0.02, indicating nominal single-reference character. However, INT-1 and INT-2 show high M values (0.11 and 0.09, respectively), suggesting significant MR character. This trend is even more pronounced in the C–H activation transition states TS-12 and TS-13, where M values of 0.28 and 0.58 reflect substantial static correlation that is not captured by the moderate T_1 values (0.024).

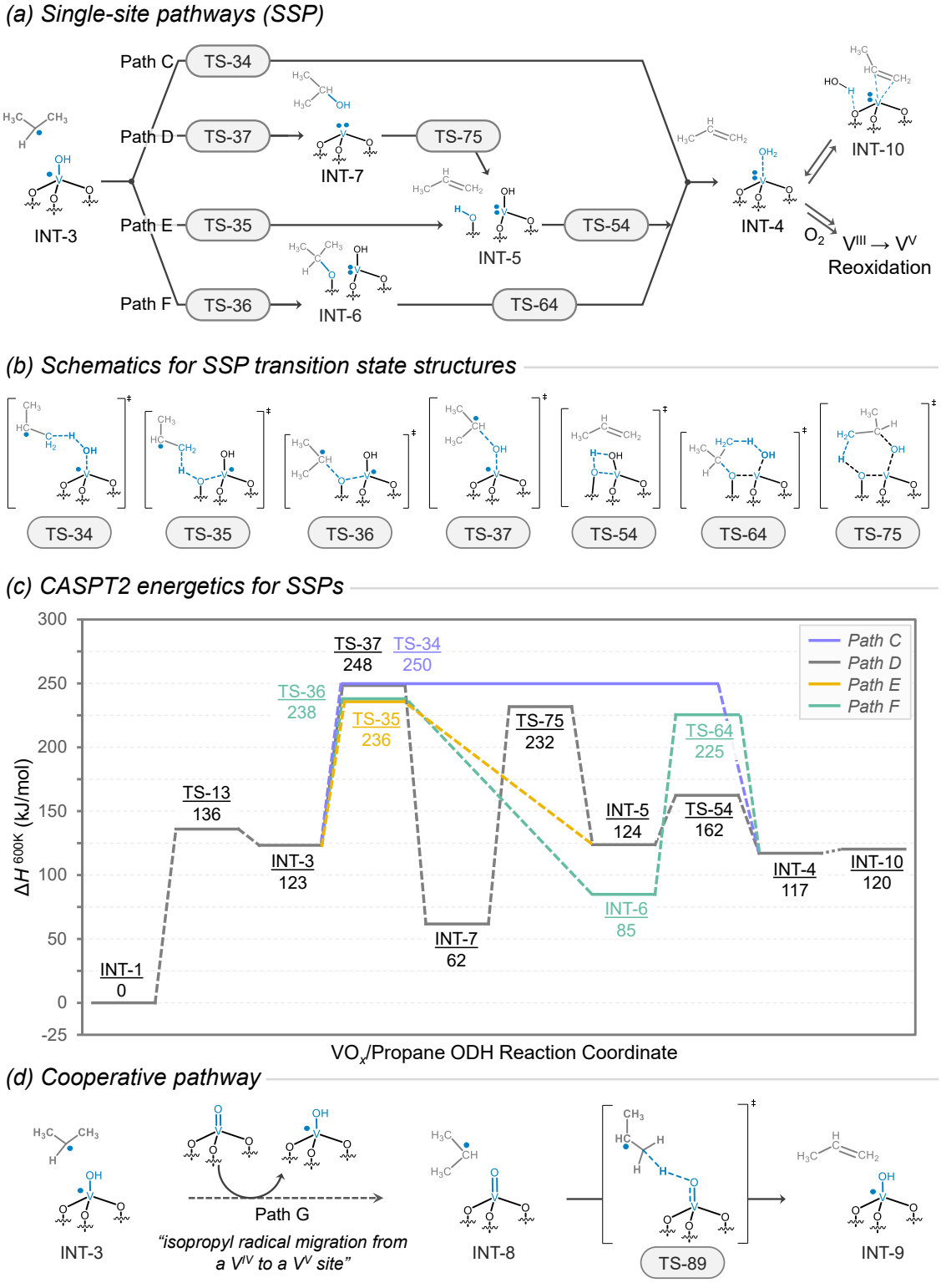

Figure 5: Isopropyl radical oxidation pathways following initial C–H activation by $O{=}VSi_7O_{12}H_7$. (a) Reaction network showing single-site pathways (Paths C to F) leading to propene. (b) Key transition structures. (c) 600 K enthalpy profile (kJ/mol) at the CASPT2/ANO-RCC-VTZP//M06-D3(0)/def2-TZVP level with a CAS(8*e*,8*o*) reference. (d) Cooperative pathway (Path G) involving radical migration (dashed arrow) from V^{IV} to V^{V}, followed by *H*-atom abstraction to form propene. Electronic states: INT-1 (closed-shell singlet), TS-13 (open-shell singlet), INT-8/INT-9/TS-89 (doublets), All other species (triplet). Adapted from Rozanska et al.[14]

Such underestimation is a known limitation of the T_1 diagnostic, as exemplified by the Cr_2 dimer, a well-known MR system with deceptively low T_1 values below 0.05.[57]

MR character diminishes markedly in the later stages of the reaction, with both T_1 and M diagnostics indicating weaker correlation for downstream intermediates and transition states. Accordingly, while MR treatment is essential for the initial C–H activation, single-reference methods are likely sufficient for describing subsequent steps of the mechanism.

IIIA.2.2. SSP Energies using MR Methods. Building on the multireference diagnostics, we employed CASPT2 and MC-PDFT to quantify the energetics of the downstream single-site pathways, focusing on key intermediates and transition states along Paths C through F. Both sets of calculations were performed using a CAS(8e,8o) reference.

CASPT2 results show that transition states associated with the second hydrogen atom abstraction from $CH_3CH(\bullet)CH_3$ (TS-34 and TS-35), radical rebound (TS-36 and TS-37), and subsequent rearrangements (TS-54, TS-64, and TS-75) span a relatively narrow range of 25 kJ/mol, with enthalpy barriers varying from 225 to 250 kJ/mol. All intermediates along these SSPs lie within approximately 60 kJ/mol of the propene-forming product INT-4. Notably, INT-7, a reduced V^{III} species coordinated to 2-propanol, emerges as the lowest-energy intermediate following INT-3, supporting the feasibility of 2-propanol formation as a byproduct in propane ODH.[24]

CASPT2 calculations identify INT-10, a previously unreported intermediate featuring a V^{III} center coordinated to propene, in contrast to the water-bound structure of INT-4. INT-10 is nearly isoenergetic with INT-4 ($\Delta\Delta H^{600K} = 3$ kJ/mol), indicating that it is thermodynamically accessible. Although we do not model the full overoxidation pathway, the persistence of adsorbed propene in INT-10 suggests a possible route for further oxidation to CO_x under O_2-rich conditions, rather than immediate desorption. As there is no experimental evidence for INT-10, we present it as a plausible but unconfirmed intermediate that may serve as a testable hypothesis for future experimental or kinetic studies aimed at understanding overoxidation pathways and improving selectivity.

To assess more computationally affordable alternatives to CASPT2, we performed MC-PDFT calculations using the same CASSCF reference. The tPBE on-top functional substantially overestimates key barrier heights, particularly for TS-54, TS-64, and TS-75, with deviations of up to 75 kJ/mol relative to CASPT2. Incorporating 25% CASSCF energy in

the hybrid tPBE0 functional improves accuracy, reducing deviations to within approximately 30 kJ/mol. Finally, the hybrid meta-on-top functional MC23 offers the best agreement, reproducing CASPT2 energetics within about 20 kJ/mol across the SSP. These results indicate that hybrid MC-PDFT functionals, provide a promising balance between accuracy and computational efficiency for these systems.

IIIA.2.3. SSP Energies using DLPNO-CCSD(T) and KS-DFT. To contextualize the CASPT2 and MC-PDFT results, we compared them with DLPNO-CCSD(T) and four KS-DFT functionals: r^{2}SCANh-D4, TPSSh-D4, M06-D3(0), and ωB97M-D4 (Table 1). DLPNO-CCSD(T) shows excellent agreement with the CASPT2 results presented in Figure 5c, with most transition state and intermediate enthalpies agreeing within $\sim$ 10 kJ/mol. Notably, the coupled-cluster results corroborate the CASPT2 prediction of INT-10, locating this previously unreported intermediate within 9 kJ/mol of INT-4. Although DLPNO-CCSD(T) significantly overestimates the barrier for the initial C–H activation, its close agreement with CASPT2 across the downstream single-site steps shows that it remains a very useful method for this part of the reaction network.

Kohn–Sham DFT methods generally capture the qualitative features of the SSP energy landscape observed with CASPT2 and DLPNO-CCSD(T), though their quantitative accuracy varies significantly (Table 1). Among the tested functionals, M06-D3(0) and r^{2}SCANh-D4 perform best for key intermediates such as INT-4, yielding enthalpies of 117 kJ/mol that match CASPT2 (117 kJ/mol) and closely align with DLPNO-CCSD(T) (120 kJ/mol). However, most functionals substantially underestimate the activation barriers for critical transition structures, including TS-34, TS-36, and TS-37, with deviations reaching up to 80 kJ/mol in the case of ωB97M-D4. While TPSSh-D4 offers more consistent barrier predictions, it tends to overestimate intermediate energies (e.g., INT-4 at 151 kJ/mol). Conversely, ωB97M-D4 systematically over-stabilizes intermediates (by $\sim$ 60–70 kJ/mol) while underestimating transition state energies (by $\sim$ 65–80 kJ/mol). Overall, while KS-DFT functionals reproduce the general energetic trends across the SSP landscape, their quantitative reliability is highly sensitive to the choice of functional.

IIIA.2.4. Mechanistic Takeaways of Single-Site Reactivity. Our analysis of single-site pathways indicates a consistent mechanistic preference for support-mediated oxidation

Table 1: 600 K enthalpies[†] (kJ/mol; INT-1 set as the reference; excludes the *RT* term) for all stationary points shown in Figures 2 and 5. Calculations were performed using the def2-TZVP basis set for single-reference methods and the ANO-RCC-VTZP basis set for multireference methods. Electronic configurations: INT-1 (closed-shell singlet); TS-12/TS-13 (open-shell singlets); INT-8/INT-9/TS-89 (doublets); All other species (triplets).

Stat. Point	Lit. Values	This Work								
	B3LYP[a]	CCSD(T)[b]	r^{2}SCANh[c]	TPSSh[c]	M06[c]	ωB97M[c]	tPBE[d]	tPBE0[d]	MC23[d]	CASPT2[d]
INT-1	0	0	0	0	0	0	0	0	0	0
INT-2	183	211	195	217	219	172	169	145	158	178
INT-3	134	189	141	162	155	136	91	146	136	123
TS-12	191	231	181	192	214	189	180	174	184	184
TS-13	117	196	125	135	161	143	86	120	144	136
INT-4	72	120	118	151	117	49	184	120	126	117
INT-5	84	132	129	163	134	57	200	133	135	124
INT-6	75	93	88	119	88	23	182	114	91	85
INT-7	39	65	59	93	62	–1	145	78	67	62
INT-10	—	129	119	151	120	58	215	151	128	120
TS-34	178	264	202	224	229	180	244	234	241	250
TS-35	184	249	201	224	232	163	242	227	228	236
TS-36	173	243	172	189	197	158	252	228	223	238
TS-37	161	252	170	190	202	167	245	221	231	248
TS-54	115	171	160	192	167	97	235	176	176	162
TS-64	181	232	196	222	220	149	300	241	228	225
TS-75	173	239	203	231	230	157	306	247	240	232
INT-8[*]	0	0	0	0	0	0	0	0	0	0
INT-9[*]	–100	–78	–60	–56	–53	–121	–39	–65	–54	–86
TS-89[*]	29	38	37	37	58	–2	–23	–17	–7	32

[†]Thermal contributions to enthalpy terms were calculated at the M06-D3(0)/def2-TZVP level; [a]Electronic energies with ZPE correction ($\approx H_{0K}$) obtained from reference;[14] [b]DLPNO-CCSD(T); [c]All DFT methods include dispersion corrections (D4 except M06-D3); [d]CASSCF (8*e*,8*o*) reference wave function.
[*]Cooperative pathway using CASSCF (9*e*,9*o*) reference wave function.

of the isopropyl radical (INT-3) on low-coverage VO_x catalysts. CASPT2 calculations show that transition states associated with support-assisted hydrogen abstraction (TS-35, Path E) and radical capture (TS-36, Path F) are favored over their V^{IV}–OH counterparts (TS-34, TS-37, Paths C and D) by at least 10 kJ/mol. Although modest, this energetic bias aligns with experimental kinetic isotope effect studies using deuterated propane[13] and underscores the critical role of the support in stabilizing intermediates and lowering barriers, consistent with the observed dependence of ODH activity on support identity.[12]

Kinetically, the initial C–H activation (TS-13) remains the rate-determining step, despite higher barriers in some downstream pathways, due to the irreversible nature of hydrogen-atom abstraction.[60] Once formed, the isopropyl radical rapidly engages in subsequent re-

actions, while the catalyst remains predominantly in its oxidized V^V state owing to fast reoxidation by molecular oxygen. This mechanistic picture is supported by microkinetic modeling, which also identifies the initial C–H activation as the rate-limiting step, with subsequent transformations proceeding quickly upon encounter with oxidized V^V sites.[24]

IIIA.3. Cooperative Reactivity of Isopropyl Radical

Beyond the single-site pathways, we explored a mechanistically distinct cooperative route for isopropyl radical conversion involving multiple VO_x sites (Path G; Figure 5d), which may become more relevant under higher vanadium loading conditions. Unlike the triplet surfaces associated with Paths C to F (Figure 5a,b), Path G proceeds on a doublet surface, where the isopropyl radical migrates from a reduced V^{IV}–OH site to a neighboring oxidized V^V=O site, forming INT-8. A second hydrogen atom abstraction from $CH_3CH(\bullet)CH_3$ via TS-89 then yields propene and a second V^{IV}–OH species (INT-9). To ensure consistent energy comparisons while avoiding size-consistency issues,[61,62] INT-8 is used as the reference for all cooperative pathway energetics.

Although we do not explicitly model V–O–V linkages, which are more likely to form at higher VO_x loadings and have been examined in previous studies,[24] the cooperative pathway explored here assumes a low-loading regime in which two nearby but isolated vanadyl sites can act in concert, following the approach used by Rozanska et al.[14] This setup allows us to directly compare the reactivity of V^V=O and V^{IV}–OH species in the subsequent oxidation of the isopropyl radical, without the added structural complexity of polymeric VO_x domains.

For this pathway, all MR calculations employed a (9e,9o) active space to account for the singly occupied molecular orbital localized on the carbon-centered radical in INT-8, in contrast to the CAS(8e,8o) used elsewhere in this study. With this reference, CASPT2 predicts a barrier of 32 kJ/mol for TS-89 (relative to INT-8) and an exothermic reaction enthalpy of –86 kJ/mol for INT-9. DLPNO-CCSD(T) yields similar results, with a barrier of 38 kJ/mol and a reaction enthalpy of –78 kJ/mol.

MC-PDFT, however, deviates from these benchmarks: all three on-top functionals predict a barrierless second HAA and reaction enthalpies between –40 and –65 kJ/mol. Among the KS-DFT functionals, r^{2}SCANh-D4 and TPSSh-D4 show the best agreement with CASPT2 and DLPNO-CCSD(T), yielding barriers of 37 kJ/mol and reaction enthalpies of –60 and –56 kJ/mol, respectively. M06-D3(0) predicts a comparable reaction enthalpy (–53 kJ/mol)

but overestimates the barrier (58 kJ/mol). In contrast, ωB97M-D4, like MC-PDFT, predicts an effectively barrierless TS-89 and a substantially overestimated exothermicity for INT-9 (–121 kJ/mol).

The cooperative pathway presents a mechanistically viable route under realistic ODH conditions. By engaging multiple active sites, Path G bypasses the high-energy V^{IV}–OH intermediates characteristic of the single-site pathways. This finding is consistent with prior studies reporting a kinetic preference for hydrogen abstraction at oxidized V^{V} centers over reduced V^{IV} sites.[14] Migration of the isopropyl radical to nearby V^{V}=O sites lowers kinetic barriers and leverages the high abundance of oxidized sites during fast catalyst reoxidation. These results suggest that optimal VO_x catalyst design should balance site density to enable cooperative effects while minimizing active site aggregation that could reduce propene selectivity.[63]

IIIB. Method Comparison Across the Reaction Network

Our analysis of the propane ODH mechanism shows that single-reference DLPNO-CCSD(T) overestimates the rate-limiting C–H activation barrier ($E_{\mathrm{app}}^{600\mathrm{K}}$ = 198 kJ/mol) relative to experiment (134 ± 4 kJ/mol),[47] due to its inability to fully capture the open-shell singlet character of TS-13. In contrast, multireference methods yield better agreement: CASPT2 predicts 138 kJ/mol, and NEVPT2 gives 115 kJ/mol. Among MC-PDFT approaches, hybrid/meta-hybrid on-top functionals improves agreement with experiment, progressing from tPBE (88 kJ/mol) to tPBE0 (122 kJ/mol) to MC23 (146 kJ/mol).

Beyond the initial C–H activation, where MR character diminishes, DLPNO-CCSD(T), CASPT2, and MC-PDFT (particularly MC23) yield comparable energetics. The mean absolute deviations (MADs) of DLPNO-CCSD(T) and MC23 from the CASPT2 reference across the single-site pathways are 8 and 9 kJ/mol, respectively (Figure 6).

Kohn-Sham DFT functionals show larger spread. For C–H activation, predicted barriers range from 125 kJ/mol (r^2SCANh-D4) to 153 kJ/mol (M06-D3(0)), with TPSSh-D4 (133 kJ/mol) and ωB97M-D4 (143 kJ/mol) in between. While ωB97M-D4 performs reasonably well for this step, it over-stabilizes downstream triplet species. In contrast, r^2SCANh-D4, TPSSh-D4, and M06-D3(0) maintain better consistency with CASPT2 across both the initial and subsequent steps (Table 1 and Figure 6).

A systematic active space analysis during the initial C–H activation shows that the mini-

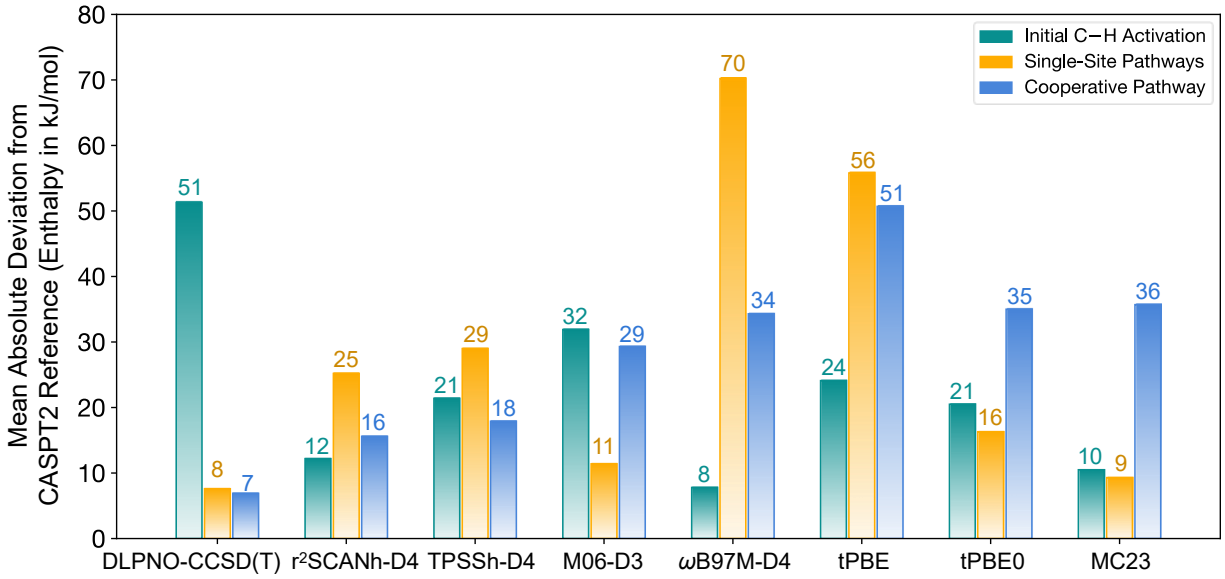

Figure 6: Mean absolute deviation (MAD) in enthalpy (kJ/mol) for various computational methods relative to CASPT2 reference calculations. Reaction pathways: Initial C–H Activation (green), Single-Site Pathways (yellow), and Cooperative Pathway (blue). All MR calculations employed an (8*e*,8*o*) active space for the first two pathways and a (9*e*,9*o*) active space for the Cooperative Pathway. Thermal contributions to enthalpy were calculated at the M06-D3(0)/def2-TZVP level for all methods.

mal CAS(6*e*,6*o*), incorporating V=O σ/π and C–H σ bonding orbitals and their antibonding counterparts, is insufficient, as indicated by significantly higher relative energies across most stationary points (Table S1). In contrast, larger spaces such as CAS(8*e*,8*o*), CAS(10*e*,10*o*), and CAS(10*e*,12*o*), where we sought to include additional V–O bonding/antibonding orbitals from the support and the vanadyl oxygen lone pair interacting with V(3*d*) orbitals (Figures S3–S8), yield more consistent results. CASPT2 demonstrates excellent stability across these spaces, with MADs relative to CAS(8*e*,8*o*) within 10 kJ/mol (Table S4). In contrast, MC-PDFT/tPBE shows MADs up to 60 kJ/mol, particularly for closed-shell species like INT-1. For MC-PDFT, "balanced" active spaces are essential—the (10*e*,10*o*) space aligns reasonably with the (8*e*,8*o*) reference, while "unbalanced" spaces such as (8*e*,10*o*) and (10*e*,12*o*) show larger deviations across multiple structures (Table S3–S4). These results emphasize the importance of selecting a minimal yet balanced active space sufficient to describe the chemical transformation when using MC-PDFT in transition-metal systems.

This difference between CASPT2 and MC-PDFT reflects a fundamental contrast: CASPT2 has a well-defined full configuration interaction (FCI) limit and exactly recovers the FCI en-

ergy when applied to an FCI reference. In contrast, MC-PDFT retains intrinsic errors due to its approximate density functional correction, even with an exact reference wave function. The distinction between CASPT2 and MC-PDFT, that the former has a FCI limit and the latter does not, might also reflect the former's apparent superior ability to "smooth over," so to speak, the differences between active spaces of different species. Note that, we were unable to control the shapes of active orbitals in all intermediates and transition states, so that calculations of some species included, for instance, active C–H σ bonding and antibonding orbitals and others did not (Figure S2). The remarkable stability of the CASPT2 relative energies to active space size suggests that these difficulties, and the resulting inconsistencies of the reference wave functions, are not too severe to be overcome with a perturbative method. On the other hand, the relative instability of the MC-PDFT relative energies suggests that this method is less able to overcome such inconsistencies in the reference wave functions.

Finally, although some KS-DFT functionals reproduce experimental barriers reasonably well, caution is warranted. For instance, r^{2}SCANh-D4 and TPSSh-D4 incorrectly predict INT-3 to be higher in energy than TS-13 and produce inconsistent relative barriers for TS-35 versus TS-36, contradicting the near-degeneracy predicted by DLPNO-CCSD(T) and CASPT2. Similarly, while ωB97M-D4 performs well for C–H activation (MAD = 8 kJ/mol vs. CASPT2), it shows deviations of up to 70 kJ/mol for downstream steps (Figure 6). These discrepancies highlight the limitations of KS-DFT in systems involving multiple spin states and emphasize the need for methods capable of reliably treating singlet, doublet, and triplet configurations across a full reaction network.

IV. Conclusions

Using a well-defined O=VSi$_7$O$_{12}$H$_7$ cluster model, we investigated the propane oxidative dehydrogenation mechanism over supported VO$_x$ catalysts. Our systematic comparison shows that the choice of electronic structure method is critical for capturing the evolving multireference (MR) character along the reaction pathway.

The initial C–H activation step exhibits strong MR character (M = 0.58 for TS-13), necessitating MR treatments to accurately reproduce experimental barriers. CASPT2 yields an activation barrier of 138 kJ/mol, closely matching the experimental value of 134 ± 4 kJ/mol, while DLPNO-CCSD(T) overestimates it at 198 kJ/mol. In later stages of the

mechanism, where MR character diminishes ($M < 0.05$), DLPNO-CCSD(T) and CASPT2 converge, with deviations reduced to within 10–15 kJ/mol.

Active space analysis confirms that a minimal CAS(6e,6o) space, comprising V=O σ/π and C–H σ bonding orbitals along with their antibonding counterparts, is insufficient. An expanded CAS(8e,8o) space, including the vanadyl oxygen lone pair, provides a reliable balance of accuracy and efficiency. Even larger active spaces do not significantly alter the activation barrier at the CASPT2 level. Thus, we recommend CAS(8e,8o) as a starting point for future MR studies of C/O–H bond activation in d^0-metal oxide systems such as VO_x.

CASPT2 results remain robust across larger active spaces. In contrast, MC-PDFT is more sensitive to active space selection, particularly with "unbalanced" spaces such as (8e,10o) or (10e,12o). These results emphasize the importance of choosing a minimal yet balanced active space, such as (8e,8o) or (10e,10o), to obtain reliable MC-PDFT energetics in transition-metal systems.

Among KS-DFT functionals, r^{2}SCANh-D4 provides the most consistent performance across the full reaction network. It yields activation barriers for the initial C–H activation step in agreement with experiment, performs well for the cooperative pathway, and maintains reasonable accuracy throughout the single-site pathway. We therefore recommend r^{2}SCANh-D4 as an initial functional choice for computationally efficient exploration of similar reactivity.

Mechanistically, our results show that catalyst structure and VO_x site density govern the accessible reaction channels. At low site-densities, support-assisted single-site pathways dominate propene production over V^{IV}–OH-mediated routes. With neighboring VO_x centers, cooperative mechanisms become accessible through isopropyl radical migration between V^{IV} and V^{V} sites.

All methods consistently indicate that initial C–H activation occurs preferentially at vanadyl rather than bridging oxygens, suggesting that heteroatom substitution at the vanadyl "E" position (E = V(–B)$_3$), rather than at bridging "B" positions, may more effectively modulate the rate-limiting C–H activation step. Studies exploring such substitution strategies to enhance reactivity are currently underway.

Acknowledgement

This work was supported by the Catalyst Design for Decarbonization Center, an Energy Frontier Research Center funded by the U.S. Department of Energy (DOE), Office of Science, Basic Energy Sciences (BES) under Award No. DE-SC0023383. Computational resources were provided by the Research Computing Center (RCC) at The University of Chicago. MM acknowledges A. Sarkar, B. Jangid, M. Hennefarth, and S. Verma for valuable technical discussions, and thanks S. Tressler for preliminary contributions to this work. LG acknowledges the Alexander von Humboldt Foundation for a Humboldt Research Award. FB acknowledges support from the Alexander von Humboldt Foundation through a Feodor Lynen Research Fellowship, from the Isaac Newton Trust through an Early Career Fellowship, and from Churchill College, Cambridge, through a Postdoctoral By-Fellowship.

Supporting Information Available

Details of active space selection and orbital choices, energy convergence with respect to active space size (PDF). The computational data supporting this study is available at Zenodo: DOI 10.5281/zenodo.15165374.

References

(1) Kung, H. H. Oxidative Dehydrogenation of Light (C2 to C4) Alkanes. *Adv. Catal.* **1994**, *40*, 1–38.

(2) Sattler, J. J. H. B.; Ruiz-Martinez, J.; Santillan-Jimenez, E.; Weckhuysen, B. M. Catalytic Dehydrogenation of Light Alkanes on Metals and Metal Oxides. *Chem. Rev.* **2014**, *114*, 10613–10653.

(3) Najari, S.; Saeidi, S.; Concepcion, P.; Dionysiou, D. D.; Bhargava, S. K.; Lee, A. F.; Wilson, K. Oxidative Dehydrogenation of Ethane: Catalytic and Mechanistic Aspects and Future Trends. *Chem. Soc. Rev.* **2021**, *50*, 4564–4605.

(4) Cavani, F.; Trifirò, F. Selective Oxidation of Light Alkanes: Interaction between the Catalyst and the Gas Phase on Different Classes of Catalytic Materials. *Catal. Today* **1999**, *51*, 561–580.

(5) Cavani, F.; Ballarini, N.; Cericola, A. Oxidative Dehydrogenation of Ethane and Propane: How Far from Commercial Implementation? *Catal. Today* **2007**, *127*, 113–131.

(6) Khodakov, A.; Olthof, B.; Bell, A. T.; Iglesia, E. Structure and Catalytic Properties of Supported Vanadium Oxides: Support Effects on Oxidative Dehydrogenation Reactions. *J. Catal.* **1999**, *181*, 205–216.

(7) Mitran, G.; Ahmed, R.; Iro, E.; Hajimirzaee, S.; Hodgson, S.; Urdă, A.; Olea, M.; Marcu, I.-C. Propane Oxidative Dehydrogenation over VO_x/SBA-15 Catalysts. *Catal. Today* **2018**, *306*, 260–267.

(8) Dinse, A.; Frank, B.; Hess, C.; Habel, D.; Schomäcker, R. Oxidative Dehydrogenation of Propane over Low-Loaded Vanadia Catalysts: Impact of the Support Material on Kinetics and Selectivity. *J. Mol. Catal. A: Chem.* **2008**, *289*, 28–37.

(9) Mars, P.; Van Krevelen, D. W. Oxidations Carried Out by Means of Vanadium Oxide Catalysts. *Chem. Eng. Sci.* **1954**, *3*, 41–59.

(10) Beck, B.; Harth, M.; Hamilton, N. G.; Carrero, C.; Uhlrich, J. J.; Trunschke, A.; Shaikhutdinov, S.; Schubert, H.; Freund, H.-J.; Schlögl, R.; et al. Partial Oxidation of Ethanol on Vanadia Catalysts on Supporting Oxides with Different Redox Properties Compared to Propane. *J. Catal.* **2012**, *296*, 120–131.

(11) Argyle, M. D.; Chen, K.; Iglesia, E.; Bell, A. T. In Situ UV–Visible Spectroscopic Measurements of Kinetic Parameters and Active Sites for Catalytic Oxidation of Alkanes on Vanadium Oxides. *J. Phys. Chem. B* **2005**, *109*, 2414–2420.

(12) Carrero, C. A.; Schloegl, R.; Wachs, I. E.; Schomäcker, R. Critical Literature Review of the Kinetics for the Oxidative Dehydrogenation of Propane over Well-Defined Supported Vanadium Oxide Catalysts. *ACS Catal.* **2014**, *4*, 3357–3380.

(13) Chen, K.; Iglesia, E.; Bell, A. T. Kinetic Isotopic Effects in Oxidative Dehydrogenation of Propane on Vanadium Oxide Catalysts. *J. Catal.* **2000**, *192*, 197–203.

(14) Rozanska, X.; Fortrie, R.; Sauer, J. Oxidative Dehydrogenation of Propane by Monomeric Vanadium Oxide Sites on Silica Support. *J. Phys. Chem. C* **2007**, *111*, 6041–6050.

(15) Vogiatzis, K. D.; Polynski, M. V.; Kirkland, J. K.; Townsend, J.; Hashemi, A.; Liu, C.; Pidko, E. A. Computational Approach to Molecular Catalysis by 3d Transition Metals: Challenges and Opportunities. *Chem. Rev.* **2018**, *119*, 2453–2523.

(16) Gaggioli, C. A.; Stoneburner, S. J.; Cramer, C. J.; Gagliardi, L. Beyond Density Functional Theory: The Multiconfigurational Approach To Model Heterogeneous Catalysis. *ACS Catal.* **2019**, *9*, 8481–8502.

(17) Vitillo, J. G.; Cramer, C. J.; Gagliardi, L. Multireference Methods are Realistic and Useful Tools for Modeling Catalysis. *Isr. J. Chem.*

2022, *62*, e202100136.

(18) Simons, M. C.; Ortuño, M. A.; Bernales, V.; Gaggioli, C. A.; Cramer, C. J.; Bhan, A.; Gagliardi, L. C–H Bond Activation on Bimetallic Two-Atom Co-M Oxide Clusters Deposited on Zr-Based MOF Nodes: Effects of Doping at the Molecular Level. *ACS Catal.* **2018**, *8*, 2864–2869.

(19) Gaggioli, C. A.; Sauer, J.; Gagliardi, L. Hydrogen Atom or Proton Coupled Electron Transfer? C–H Bond Activation by Transition-Metal Oxides. *J. Am. Chem. Soc.* **2019**, *141*, 14603–14611.

(20) Vitillo, J. G.; Lu, C. C.; Bhan, A.; Gagliardi, L. Comparing the Reaction Profiles of Single Iron Catalytic Sites in Enzymes and in Reticular Frameworks for Methane-to-methanol Oxidation. *Cell Rep. Phys. Sci.* **2023**, *4*, 101422.

(21) Khan, S. N.; Quebedeaux, B.; Miliordos, E. Selective Conversion of Methane to Methanol Facilitated by Molecular Metal–methoxy Complexes via a Self-correcting Chemical Cycle. *Phys. Chem. Chem. Phys.* **2024**, *26*, 23136–23143.

(22) Maity, B.; Scott, T. R.; Stroscio, G. D.; Gagliardi, L.; Cavallo, L. The Role of Excited States of $LNi^{II/III}$(Aryl)(Halide) Complexes in Ni–Halide Bond Homolysis in the Arylation of C_{sp^3}–H Bonds. *ACS Catal.* **2022**, *12*, 13215–13224.

(23) He, N.; Nakatani, N.; Hada, M. How Does Multi-reference Computation Change the Catalysis Chemistry? DFT and CASPT2 Studies of the Cu-catalysed Coupling Reactions Between Aryl Iodides and β-Diketones. *Phys. Chem. Chem. Phys.* **2023**, *25*, 28871–28884.

(24) Rozanska, X.; Fortrie, R.; Sauer, J. Size-Dependent Catalytic Activity of Supported Vanadium Oxide Species: Oxidative Dehydrogenation of Propane. *J. Am. Chem. Soc.* **2014**, *136*, 7751–7761.

(25) Cheng, M.-J.; Chenoweth, K.; Oxgaard, J.; van Duin, A.; Goddard, W. A. Single-Site Vanadyl Activation, Functionalization, and Reoxidation Reaction Mechanism for Propane Oxidative Dehydrogenation on the Cubic V_4O_{10} Cluster. *J. Phys. Chem. C* **2007**, *111*, 5115–5127.

(26) Redfern, P. C.; Zapol, P.; Sternberg, M.; Adiga, S. P.; Zygmunt, S. A.; Curtiss, L. A. Quantum Chemical Study of Mechanisms for Oxidative Dehydrogenation of Propane on Vanadium Oxide. *J. Phys. Chem. B* **2006**, *110*, 8363–8371.

(27) Wang, Y.; Hu, P.; Yang, J.; Zhu, Y.-A.; Chen, D. C–H Bond Activation in Light Alkanes: A Theoretical Perspective. *Chem. Soc. Rev.* **2021**, *50*, 4299–4358.

(28) Lee, C.; Yang, W.; Parr, R. G. Development of the Colle-Salvetti Correlation-Energy Formula into a Functional of the Electron Density. *Phys. Rev. B Condens. Matter* **1988**, *37*, 785–789.

(29) Becke, A. D. Density-Functional Thermochemistry. III. The Role of Exact Exchange. *J. Chem. Phys.* **1993**, *98*, 5648–5652.

(30) Pykavy, M.; Van Wüllen, C. A Systematic Quantum Chemical Investigation of the C–H Bond Activation in Methane by Gas Phase Vanadium Oxide Cation VO^+. *J. Comput. Chem.* **2007**, *28*, 2252–2259.

(31) Rozanska, X.; Sauer, J. Oxidative Conversion of C1–C3 Alkanes by Vanadium Oxide Catalysts. DFT Results and Their Accuracy. *Int. J. Quantum Chem.* **2008**, *108*, 2223–2229.

(32) Roos, B. O.; Taylor, P. R.; Sigbahn, P. E. A Complete Active Space SCF Method (CASSCF) using a Density Matrix Formulated Super-CI Approach. *Chem. Phys.* **1980**, *48*, 157–173.

(33) Andersson, K.; Malmqvist, P.-Å.; Roos, B. O. Second-Order Perturbation Theory with a Complete Active Space Self-Consistent Field Reference Function. *J. Chem. Phys.* **1992**, *96*, 1218–1226.

(34) Li Manni, G.; Carlson, R. K.; Luo, S.; Ma, D.; Olsen, J.; Truhlar, D. G.; Gagliardi, L. Multi-configuration Pair-Density Functional Theory. *J. Chem. Theory Comput.* **2014**, *10*, 3669–3680.

(35) Riplinger, C.; Sandhoefer, B.; Hansen, A.; Neese, F. Natural Triple Excitations in Local Coupled Cluster Calculations with Pair Natural Orbitals. *J. Chem. Phys.* **2013**, *139*, 134101.

(36) Murugavel, R.; Voigt, A.; Walawalkar, M. G.; Roesky, H. W. Hetero- and Metallasiloxanes Derived from Silanediols, Disilanols, Silanetriols, and Trisilanols. *Chem. Rev.* **1996**, *96*, 2205–2236.

(37) Magg, N.; Immaraporn, B.; Giorgi, J. B.; Schroeder, T.; Bäumer, M.; Döbler, J.; Wu, Z.; Kondratenko, E.; Cherian, M.; Baerns, M.; et al. Vibrational Spectra of Alumina- and Silica-Supported Vanadia Revisited: An Experimental and Theoretical Model Catalyst Study. *J. Catal.* **2004**, *226*, 88–100.

(38) Goodrow, A.; Bell, A. T. A Theoretical Investigation of the Selective Oxidation of Methanol to Formaldehyde on Isolated Vanadate Species Supported on Silica. *J. Phys. Chem. C* **2007**, *111*, 14753–14761.

(39) Döbler, J.; Pritzsche, M.; Sauer, J. Oxidation of Methanol to Formaldehyde on Supported Vanadium Oxide Catalysts Compared to Gas Phase Molecules. *J. Am. Chem. Soc.* **2005**, *127*, 10861–10868.

(40) Wang, C.-B.; Deo, G.; Wachs, I. E. Characterization of Vanadia Sites in V-Silicalite, Vanadia-Silica Cogel, and Silica-Supported Vanadia Catalysts: X-Ray Powder Diffraction, Raman Spectroscopy, Solid-State ^{51}V NMR, Temperature-Programmed Reduction, and Methanol Oxidation Studies. *J. Catal.* **1998**, *178*, 640–648.

(41) Keller, D. E.; Visser, T.; Soulimani, F.; Koningsberger, D. C.; Weckhuysen, B. M. Hydration Effects on the Molecular Structure of Silica-Supported Vanadium Oxide Catalysts: A Combined IR, Raman, UV-vis and EXAFS Study. *Vib. Spectrosc.* **2007**, *43*, 140–151.

(42) Seetula, J. A.; Slagle, I. R. Kinetics and Thermochemistry of the R + HBr $\rightleftharpoons$ RH + Br (R = n-C_3H_7, isoC_3H_7, n-C_4H_9, isoC_4H_9, sec$-C_4H_9$ or tert$-C_4H_9$) Equilibrium. *J. Chem. Soc., Faraday Trans.* **1997**, *93*, 1709–1719.

(43) Kozuch, S.; Shaik, S. How to Conceptualize Catalytic Cycles? The Energetic Span Model. *Acc. Chem. Res.* **2011**, *44*, 101–110.

(44) Mao, Z.; Campbell, C. T. Apparent Activation Energies in Complex Reaction Mechanisms: A Simple Relationship via Degrees of Rate Control. *ACS Catal.* **2019**, *9*, 9465–9473.

(45) Kondratenko, E.; Cherian, M.; Baerns, M.; Su, D.; Schlogl, R.; Wang, X.; Wachs, I. Oxidative Dehydrogenation of Propane Over V/MCM-41 Catalysts: Comparison of O_2 and N_2O as Oxidants. *J. Catal.* **2005**, *234*, 131–142.

(46) Karakoulia, S.; Triantafyllidis, K.; Tsilomelekis, G.; Boghosian, S.; Lemonidou, A. Propane Oxidative Dehydrogenation Over Vanadia Catalysts Supported on Mesoporous Silicas with Varying Pore Structure and Size. *Catal. Today* **2009**, *141*, 245–253.

(47) Gruene, P.; Wolfram, T.; Pelzer, K.; Schlögl, R.; Trunschke, A. Role of Dispersion of Vanadia on SBA-15 in the Oxidative Dehydrogenation of Propane. *Catal. Today* **2010**, *157*, 137–142.

(48) Galameau, A.; Cambon, H.; Martin, T.; De Ménorval, L.-C.; Brunel, D.; Di Renzo, F.; Fajula, F. *Nanoporous Materials III, Proceedings of the 3rdInternational Symposium on Nanoporous Materials*; Elsevier, 2002; p 395–402.

(49) Mandal, M.; Cramer, C. J.; Truhlar, D. G.; Sauer, J.; Gagliardi, L. Structure and Reactivity of Single-site Vanadium Catalysts Supported on Metal–Organic Frameworks. *ACS Catal.* **2020**, *10*, 10051–10059.

(50) Mandal, M.; Buss, J. A.; Chen, S.-J.; Cramer, C. J.; Stahl, S. S. Mechanistic In-

sights into Radical Formation and Functionalization in Copper/*N*-Fluorobenzenesulfonimide Radical-relay Reactions. *Chem. Sci.* **2024**, *15*, 1364–1373.

(51) Han, R.; Luber, S. Complete Active Space Analysis of a Reaction Pathway: Investigation of the Oxygen–Oxygen Bond Formation. *J. Comput. Chem.* **2020**, *41*, 1586–1597.

(52) Marenich, A. V.; Jerome, S. V.; Cramer, C. J.; Truhlar, D. G. Charge Model 5: An Extension of Hirshfeld Population Analysis for the Accurate Description of Molecular Interactions in Gaseous and Condensed Phases. *J. Chem. Theory Comput.* **2012**, *8*, 527–541.

(53) Pandharkar, R.; Hermes, M. R.; Truhlar, D. G.; Gagliardi, L. A New Mixing of Nonlocal Exchange and Nonlocal Correlation with Multiconfiguration Pair-Density Functional Theory. *J. Phys. Chem. Lett.* **2020**, *11*, 10158–10163.

(54) Bao, J. J.; Zhang, D.; Zhang, S.; Gagliardi, L.; Truhlar, D. G. A Hybrid Meta On-top Functional for Multiconfiguration Pair-Density Functional Theory. *Proc. Natl. Acad. Sci. U.S.A.* **2024**, *122*, e2419413121.

(55) Chen, K.; Khodakov, A.; Yang, J.; Bell, A. T.; Iglesia, E. Isotopic Tracer and Kinetic Studies of Oxidative Dehydrogenation Pathways on Vanadium Oxide Catalysts. *J. Catal.* **1999**, *186*, 325–333.

(56) Lee, T. J.; Taylor, P. R. A Diagnostic for Determining the Quality of Single-Reference Electron Correlation Methods. *Int. J. Quantum Chem.* **1989**, *36*, 199–207.

(57) Jiang, W.; DeYonker, N. J.; Wilson, A. K. Multireference Character for 3d Transition-Metal-Containing Molecules. *J. Chem. Theory Comput.* **2012**, *8*, 460–468.

(58) Tishchenko, O.; Zheng, J.; Truhlar, D. G. Multireference Model Chemistries for Thermochemical Kinetics. *J. Chem. Theory Comput.* **2008**, *4*, 1208–1219.

(59) Wardzala, J. J.; King, D. S.; Ogunfowora, L.; Savoie, B.; Gagliardi, L. Organic Reactivity Made Easy and Accurate with Automated Multireference Calculations. *ACS Cent. Sci.* **2024**, *10*, 833–841.

(60) Chen, K.; Bell, A. T.; Iglesia, E. Kinetics and Mechanism of Oxidative Dehydrogenation of Propane on Vanadium, Molybdenum, and Tungsten Oxides. *J. Phys. Chem. B* **2000**, *104*, 1292–1299.

(61) Rintelman, J. M.; Adamovic, I.; Varganov, S.; Gordon, M. S. Multireference Second-order Perturbation Theory: How Size Consistent is "Almost Size Consistent". *J. Chem. Phys.* **2005**, *122*, 044105.

(62) In the cooperative pathway, the isopropyl radical migrates from a reduced V^{IV} site to an adjacent oxidized V^{V} site, yielding INT-8 from INT-3. While INT-3 could, in principle, serve as the energy reference (as employed elsewhere in this study), this would require performing arithmetic combination of energy terms. Specifically, given that E(INT-3) = $E(V^{IV})$ + E(isopropyl radical), the energy of INT-8 can be expressed in terms of INT-3 as follows: E(INT-8) = E(INT-3) + $E(V^{V})$ – $E(V^{IV})$. However, while size-consistent methods allow for such energy combinations, size-inconsistent methods do not. To avoid these complications and ensure direct comparability with size-inconsistent methods, the reference point in this pathway is set at INT-8, that is, after the radical migration has occurred.

(63) Mitran, G.; Ahmed, R.; Iro, E.; Hajimirzaee, S.; Hodgson, S.; Urdă, A.; Olea, M.; Marcu, I.-C. Propane Oxidative Dehydrogenation Over VO_x/SBA-15 Catalysts. *Catal. Today* **2018**, *306*, 260–267.

TOC Graphic

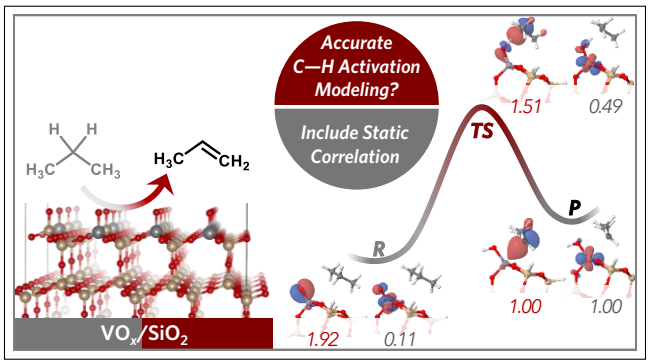
Accurate C—H Activation Modeling?
Include Static Correlation
TS
R
P
1.51
0.49
1.00
1.00
1.92
0.11
VOx/SiO2